

Process tomography of ion trap quantum gates

M. Riebe,¹ K. Kim,¹ P. Schindler,¹ T. Monz,¹ P. O. Schmidt,¹
T. K. Körber,^{1,2} W. Hänsel,¹ H. Häffner,^{1,2} C. F. Roos,^{1,2} and R. Blatt^{1,2}

¹*Institut für Experimentalphysik, Universität Innsbruck, Technikerstrasse 25, A-6020 Innsbruck, Austria*

²*Institut für Quantenoptik und Quanteninformation der Österreichischen Akademie der Wissenschaften, Technikerstr. 21a, A-6020 Innsbruck, Austria*

(Dated: September 11, 2018)

A crucial building block for quantum information processing with trapped ions is a controlled-NOT quantum gate. In this paper, two different sequences of laser pulses implementing such a gate operation are analyzed using quantum process tomography. Fidelities of up to 92.6(6) % are achieved for single gate operations and up to 83.4(8) % for two concatenated gate operations. By process tomography we assess the performance of the gates for different experimental realizations and demonstrate the advantage of amplitude-shaped laser pulses over simple square pulses. We also investigate whether the performance of concatenated gates can be inferred from the analysis of the single gates.

PACS numbers: 03.65.Wj, 03.67.Lx, 32.80.Qk

Processing information with well-controlled quantum systems has the fascinating perspective of being much more powerful than classical computers for certain applications. A promising candidate for the experimental realization of quantum computing are strings of ions stored in linear Paul traps [1] as recently demonstrated by various key experiments, including the preparation of multi-particle entangled states [2, 3], quantum teleportation [4, 5] and quantum error correction [6]. Quantum information processing depends on the ability to implement single qubit rotations and most importantly an entangling two-qubit quantum gate [7, 8, 9, 10]. Proper characterization and understanding of the action of gate operations and their imperfections is of vital importance in order to successfully apply them in complex computations.

Generally, the implementations of quantum gates are imperfect due to decoherence and various systematic error sources present in experimental setups. A proper description of such an operation which accounts for the possibly non-unitary evolution of the qubits is provided by quantum process tomography [11, 12]. Process tomography has already been applied for characterizing quantum gates in NMR and linear-optics quantum computing [13, 14, 15]. Here, we show that process tomography is a valuable tool for comparing different ion trap quantum gate implementations and optimizing the experimental parameters. This way, we were able to improve our controlled-NOT (CNOT) gate fidelity from 71 % [7] to almost 93 %. Moreover, the action of two successively applied gate operations is investigated and compared to the predictions from the single gate tomography result.

We realize entangling gates between $^{40}\text{Ca}^+$ ions held in a linear trap [16]. Quantum information is stored in superpositions of the $|S\rangle \equiv S_{1/2}(m = -1/2)$ ground state and the metastable $|D\rangle \equiv D_{5/2}(m = -1/2)$ state and is manipulated by laser pulses at a wavelength of 729 nm

exciting the electric quadrupole transition between those states. A focus size smaller than the inter-ion distance and precise control of the focus position allows us to address single qubits. Detection of the qubit's quantum state is achieved by scattering light on the $S_{1/2} \leftrightarrow P_{1/2}$ dipole transition and detecting the presence or absence of resonance fluorescence of the individual ions with a CCD-camera. The oscillations of the ions in the harmonic trap potential are described by normal modes and give rise to sidebands in the spectrum of the $S_{1/2} \leftrightarrow D_{5/2}$ transition. For coherent state manipulation, only the quantum states $|n\rangle$ of the axial center-of-mass mode at a frequency $\omega_z = 2\pi \cdot 1.36$ MHz are relevant. Here, n denotes the number of vibrational quanta. Quantum information processing is implemented by (a) laser pulses on the carrier transitions $|S, n\rangle \leftrightarrow |D, n\rangle$ realizing single qubit operations on the ion qubits and (b) laser pulses on the first blue sideband inducing transitions between the states $|S, n\rangle$ and $|D, n+1\rangle$ which connect the internal state of the ions and the state of the vibrational mode. The latter operation allows us to implement an entangling interaction between ion qubits [1]. A more detailed account of our experimental setup can be found in Ref. [16].

Cirac-Zoller controlled-NOT gate operations between two ion qubits are implemented by the pulse sequences shown in Tab. I. In both sequences, the quantum state of the control qubit 2 is first mapped to the vibrational mode (SWAP I), which is cooled to its ground state prior to the operation. Then a CNOT operation is performed between the vibrational mode and the target ion qubit 1. Finally the state of the vibrational mode is mapped back onto the control qubit (SWAP II), restoring its quantum state and returning the vibrational mode to its ground state. Both pulse sequences differ only in the way the phase gate sequence is implemented. The ideal unitary

evolution realized by the first pulse sequence (A) is [7]

$$U_{\text{CNOT}}^{(\text{A})} = \begin{pmatrix} 0 & i & 0 & 0 \\ -i & 0 & 0 & 0 \\ 0 & 0 & -1 & 0 \\ 0 & 0 & 0 & -1 \end{pmatrix} \\ = -\frac{1}{2} \left(\hat{I} \otimes \hat{I} - \hat{Z} \otimes \hat{I} + \hat{I} \otimes \hat{Y} + \hat{Z} \otimes \hat{Y} \right), \quad (1)$$

where the matrix is written in the product basis $\{|DD\rangle, |DS\rangle, |SD\rangle, |SS\rangle\}$ and expressed in terms of the Pauli operators \hat{X} , \hat{Y} , \hat{Z} and the identity \hat{I} . In this sequence the state of target ion 1 is flipped whenever control ion 2 is in state $|D\rangle$ (the order of the ions is |ion 2, ion 1>). The unitary evolution of the second pulse sequence (B) is [17]

$$U_{\text{CNOT}}^{(\text{B})} = \hat{U}_Z \cdot \begin{pmatrix} 1 & 0 & 0 & 0 \\ 0 & 1 & 0 & 0 \\ 0 & 0 & 0 & i \\ 0 & 0 & -i & 0 \end{pmatrix} \\ = \frac{1}{2} \hat{U}_Z \cdot \left(\hat{I} \otimes \hat{I} + \hat{Z} \otimes \hat{I} - \hat{I} \otimes \hat{Y} + \hat{Z} \otimes \hat{Y} \right). \quad (2)$$

Here the state of the target ion 1 is flipped whenever the control ion 2 is in $|S\rangle$. This pulse sequence shows the desired unitary evolution if an additional rotation $\hat{U}_Z = \exp[-i \cdot (1 - 1/\sqrt{8})\pi \cdot \hat{Z}] \otimes \exp[-i \cdot \pi/\sqrt{8} \cdot \hat{Z}]$ is applied. If this CNOT pulse sequence is embedded in a larger algorithm, the additional rotation can be taken into account by shifting the phase of every subsequent pulse by $\Delta\phi = -1/\sqrt{2} \cdot \pi$ on the control ion and by $\Delta\phi = +1/\sqrt{2} \cdot \pi$ on the target ion. As can be seen from Tab. I, pulse sequence (B) is shorter in terms of total length of the sideband pulses than sequence (A).

Description	Seq. (A)	Seq. (B)
SWAP I	$R_2^+(\pi, 0)$	$R_2^+(\pi, 0)$
Ramsey I	$R_1(\pi/2, 0)$	$R_1(\pi/2, 0)$
Phase gate	$R_1^+(\pi, \pi/2)$	$R_1^+(\pi/2, \pi)$
	$R_1^+(\pi/\sqrt{2}, 0)$	$R_1^+(\sqrt{2}\pi, \pi/2)$
	$R_1^+(\pi, \pi/2)$	$R_1^+(\pi/2, 0)$
	$R_1^+(\pi/\sqrt{2}, 0)$	
Ramsey II	$R_1(\pi/2, \pi)$	$R_1(\pi/2, (1/\sqrt{2} - 1)\pi)$
SWAP II	$R_2^+(\pi, \pi)$	$R_2^+(\pi, \pi)$

TABLE I: Two sequences of laser pulses for implementing a CNOT gate operation. Laser pulses applied to the i -th ion on the carrier transition are denoted by $R_i(\theta, \phi)$ and pulses on the blue sideband transition by $R_i^+(\theta, \phi)$, where $\theta = \Omega \cdot t$ denotes the pulse area in terms of the Rabi frequency Ω , the pulse length t and its phase ϕ [18].

Due to systematic imperfections and decoherence the actual evolution in our experiment will deviate from the ideal unitary evolution given in (1) and (2). An important systematic error in our setup is imperfect addressing. Every laser pulse which addresses one of the ions

also slightly affects the neighboring ion qubits, due to the finite size of the laser beam focus. In terms of the ratio of Rabi frequencies between the addressed and the neighboring ions, this error is on the order of 2-3 %. Furthermore, due to decoherence the output state after application of an operation will in general be a mixed state. The major sources of decoherence in our experimental setup are fluctuations of the laser frequency and the ambient magnetic field [19].

The experimentally realized quantum gate including error sources is properly described by a completely positive map \mathcal{E} . For an input state ρ , the output state $\mathcal{E}(\rho)$ can be written in the operator sum representation [11] as

$$\mathcal{E}(\rho) = \sum_{m,n=0}^{4^N-1} \chi_{mn} \hat{A}_m \rho \hat{A}_n^\dagger, \quad (3)$$

where N is the number of qubits and the \hat{A}_m are operators forming a basis in the space of $2^N \times 2^N$ -matrices. The *process matrix* χ contains complete information about the investigated process including the influence of the environment on the qubits. The matrix χ can be experimentally obtained by employing quantum process tomography. This procedure requires 4^N input states $\rho_{in,i}$ which are linearly independent. For every input state, the output state $\mathcal{E}(\rho_{in,i})$ has to be determined by quantum state tomography. From this set of data the process matrix χ can be obtained by inverting the relation in (3). However, to avoid unphysical results caused by quantum noise in the measurement process, we employ an iterative maximum likelihood algorithm [20] in order to find the physical process \mathcal{E} which most likely generated the measured data set. We choose the products of the single qubit states $|\psi_1\rangle = |S\rangle$, $|\psi_2\rangle = |D\rangle$, $|\psi_3\rangle = (|D\rangle + i|S\rangle)/\sqrt{2}$ and $|\psi_4\rangle = (|D\rangle + |S\rangle)/\sqrt{2}$ as the 16 input states necessary for a tomography of our two qubit quantum gates. Quantum state tomography of a two qubit system then requires measurements in nine different product state bases [18]. This results in a total of $16 \times 9 = 144$ different measurement settings. Every expectation value is determined through 100-250 individual experiments at a rate of 50 experiments/s which requires 5-12 minutes of measurement time to gather all data necessary for the estimation of χ .

Quantum process tomography was carried out for the operations implemented by pulse sequences (A) and (B) shown in Tab. I. The duration of the complete CNOT pulse sequence was $T_{\text{Gate}} = 615 \mu\text{s}$ for sequence (A) and $T_{\text{Gate}} = 502 \mu\text{s}$ for (B), which is mainly determined by the Rabi frequency on the blue sideband at $\Omega_{\text{BSB}} = 2\pi \cdot 4.4 \text{ kHz}$. The resulting estimated process matrix χ_{cnot} for pulse sequence (B) is shown in Fig. 1.

The process matrix allows us to calculate various measures which characterize the performance of the gate operation. We can directly calculate the *process fidelity*

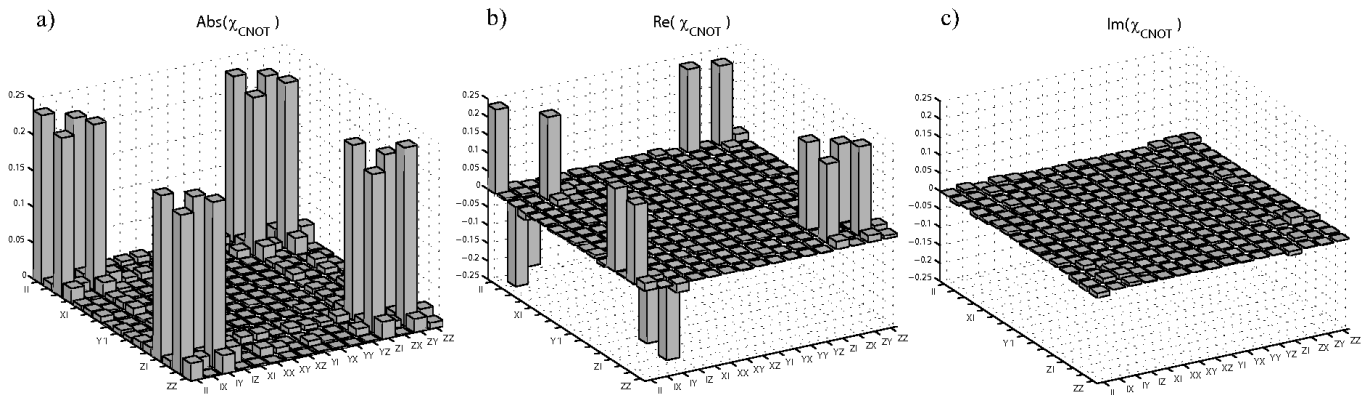


FIG. 1: Process matrix obtained by process tomography of a gate operation implemented by pulse sequence (B) in Tab. I. The absolute value, real part and imaginary part of χ_{CNOT} are shown in a), b) and c) respectively. The matrix is expressed in terms of the products of the identity \hat{I} and the Pauli operators \hat{X} , \hat{Y} and \hat{Z} . In order to compensate for the rotation \hat{U}_Z the phase of all tomography pulses was shifted appropriately.

$F_p = \text{tr}(\chi_{\text{id}} \cdot \chi_{\text{CNOT}})$, which is the overlap of our experimentally obtained χ_{CNOT} with the ideal process matrix χ_{id} derived from the unitary evolution of the gate given in (1) and (2), respectively. Furthermore, using Eq. (3) we can predict the output state of the experimental gate operation for an arbitrary input state. This enables us to investigate the gate performance for a large number of numerically generated input states, similar to the analysis done for an optical CNOT gate in Ref. [14]. We do this by analyzing the calculated output states in terms of their overlap $F = \langle \psi_{\text{id,out}} | \mathcal{E}(\rho) | \psi_{\text{id,out}} \rangle$ with the ideal output states $|\psi_{\text{id,out}}\rangle$, their normalized linear entropy $S_{\text{lin}} = 4/3 \cdot \text{tr}(1 - \mathcal{E}(\rho)^2)$ and the change in entanglement from the input to the output states given by the change in the concurrence, i.e. the difference $\Delta C = C(\mathcal{E}(\rho)) - C(\rho)$ [21]. For $5 \cdot 10^4$ randomly chosen pure input states drawn

from the Haar measure on the unitary group $U(4)$, we carry out such an analysis using the results of the process tomography for the two types of quantum gates described above. We characterize the gate performance by calculating the mean fidelity F_{mean} , the mean linear entropy \hat{S}_{lin} and by searching for the maximum increase in entanglement $\max(\Delta C)$. The results for a single gate operation are shown in Tab. II (rows 1,2). Pulse sequence (B) shows a slightly better performance than sequence (A) probably due to the 20 % shorter phase gate sequence, which reduces the influence of decoherence. Furthermore, errors due to imperfect addressing will partially cancel in phase gate sequence (B), since the two $\pi/2$ -pulses are applied with a relative phase of π .

We used this kind of analysis to assess the influence of amplitude pulse shaping on the gate performance. Exciting the blue sideband transition with square laser pulses causes off-resonant excitation of the carrier transition degrading the performance of the quantum gate. If higher gate speeds were to be achieved by using higher sideband Rabi frequencies [22], this effect would become increasingly harmful. However, we largely suppress off-resonant excitations by adiabatically switching on and off the laser pulses [23]. We demonstrated this by first carrying out a process tomography of gate pulse sequence (B) for $T_{\text{gate}} = 520 \mu\text{s}$ using shaped pulses, that were adiabatically switched on and off with a rise and fall time of $5 \mu\text{s}$ (the standard setting for all reported results). Then we carried out another gate tomography using simple square pulses. As can be seen from the results in Tab. II (rows 3,4), the use of shaped pulses considerably improves the gate performance compared with the result [7] with square pulses.

Quantum algorithms will generally contain multiple quantum gates, which are successively applied to a qubit register. The question arises whether the performance of such a series of quantum gates can be inferred from the

Seq.	F_p in %	F_{mean} in %	\hat{S}_{lin}	$\max(\Delta C)$	Description	
1	A	88.8(7)	91.0(6)	0.20(1)	0.86(2)	single gate $\mathcal{E}_{\text{CNOT(A)}}$
2	B	90.8(6)	92.6(6)	0.17(1)	0.84(2)	single gate $\mathcal{E}_{\text{CNOT(B)}}$
3	A	87.7(7)	90.1(6)	0.21(1)	0.81(2)	with pulse shaping
4	A	75(1)	80(1)	0.39(2)	0.70(3)	no pulse shaping
5	AA	79(1)	83.4(8)	0.34(2)	-	$\mathcal{E}_{2 \times \text{CNOT(A)}}$
6	A	82.8	86.2	0.30	-	$\mathcal{E}_{\text{CNOT(A)}} \circ \mathcal{E}_{\text{CNOT(A)}}$
7	BB	72(1)	77.4(8)	0.41(1)	-	$\mathcal{E}_{2 \times \text{CNOT(B)}}$
8	B	79.8	83.8	0.34	-	$\mathcal{E}_{\text{CNOT(B)}} \circ \mathcal{E}_{\text{CNOT(B)}}$

TABLE II: Performance of gate operations for different experimental realizations. The mean fidelity F_{mean} , the mean linear entropy \hat{S}_{lin} and the maximum change in entanglement $\max(\Delta C)$ were inferred from an ensemble of $5 \cdot 10^4$ random states. The quoted errors are due to quantum projection noise [18]. For the results in rows 1,2,5-8 the blue sideband Rabi frequency was set to $\Omega_{\text{BSB}} = 2\pi \cdot 4.4 \text{ kHz}$. In rows 3,4 a higher Rabi frequency of $\Omega_{\text{BSB}} = 2\pi \cdot 5.3 \text{ kHz}$ was chosen. Rows 5,7 contain the results for the tomographies of two concatenated gates. Additionally, rows 6,7 show the results predicted from the single gate analysis.

knowledge of the single-gate performances in experimental implementations of an algorithm. We investigated this issue by comparing the result of a process tomography of two concatenated CNOT gates with the predictions inferred from the single gate tomography, for the same set of experimental parameters. Ideally, two concatenated CNOT yield the identity, $(U_{\text{CNOT}})^2 = I$. The measured process matrix $\chi_{2 \times \text{CNOT}}$ is shown in Fig. 2. As expected, the dominant element of $\chi_{2 \times \text{CNOT}}$ is the II, II -element. We determined the process fidelity, mean fidelity and mean entropy of the operation described by $\chi_{2 \times \text{CNOT}}$. For comparison, we calculated the same quantities for the process $\mathcal{E}_{\text{CNOT}} \circ \mathcal{E}_{\text{CNOT}}$, where $\mathcal{E}_{\text{CNOT}}$ was obtained from the single gate process tomography. The results are shown in Tab. II (rows 5-8). In general, one would expect both methods to yield the same results if the dynamics of interaction between the qubits and the environment was Markovian, thus producing uncorrelated errors in both gates. In our experiment, we attribute the observed discrepancy to low-frequency magnetic noise giving rise to magnetic fields that are constant over the course of the double gate sequence but vary from experiment to experiment. In addition to characterizing the performance of gates within larger blocks, concatenating quantum gates might be useful for amplifying tiny errors in high-quality gates to a measurable size.

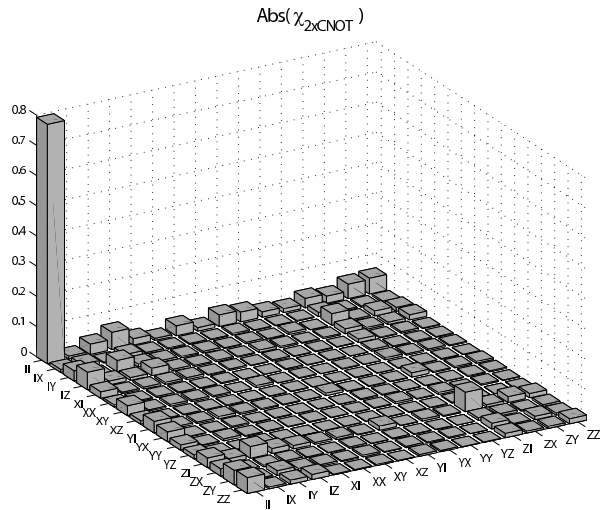


FIG. 2: Absolute value of the measured process matrix resulting from two gate operations successively applied to a pair of ion qubits. Ideally the process matrix should only contain the II, II -element. The height of the II, II -element in the measured process matrix of 79.3 % directly gives the process fidelity.

The presented work demonstrates quantum process tomography to be a valuable tool for assessing the performance of the fundamental operations of ion trap quantum computers. Since a complete tomographic data set can be taken in a comparably short amount of time, it is easily possible to compare the performance of quantum

gates for different pulse sequences and experimental parameters. This has been illustrated by showing that adiabatically switching on and off laser pulses instead of using rectangular shaped pulses make higher gate speeds possible while preserving high gate fidelities. This technique and careful optimization of the experimental parameters using process tomography helped to significantly improve the gate fidelity compared with earlier results [7, 16]. The results of the concatenated gate tomography demonstrate the importance of analyzing experimental quantum gate implementations not only as isolated objects but also within a larger gate sequence. We expect that this technique will have considerable impact on estimating the overall performance of future quantum computers.

We acknowledge support by the Austrian Science Fund (FWF), by the European Commission (QGATES, SCALA, CONQUEST networks) and by the Institut für Quanteninformation GmbH. This material is based on work supported in part by the US Army Research Office. K. Kim acknowledges funding by the Lise-Meitner program of the FWF. We acknowledge P. Pham's contribution to the development of a source of shaped RF pulses. H. Häffner acknowledges useful discussions with H. De Raedt.

-
- [1] J. I. Cirac and P. Zoller, Phys. Rev. Lett. **74**, 4091 (1995).
 - [2] H. Häffner et al., Nature **438**, 643 (2005).
 - [3] D. Leibfried et al., Nature **438**, 639 (2005).
 - [4] M. Riebe et al., Nature **429**, 734 (2004).
 - [5] M. D. Barrett et al., Nature **429**, 737 (2004).
 - [6] J. Chiaverini et al., Nature **432**, 602 (2004).
 - [7] F. Schmidt-Kaler et al., Nature **422**, 408 (2003).
 - [8] D. Leibfried et al., Nature **422**, 412.
 - [9] P. C. Haljan et al., Phys. Rev. A **72**, 062316 (2005).
 - [10] J. P. Home et al., New J. Phys. **8**, 188(2006).
 - [11] I. L. Chuang and M. A. Nielsen, J. Mod. Opt. **44**, 2455 (1997).
 - [12] J. F. Poyatos, J. I. Cirac, and P. Zoller, Phys. Rev. Lett. **78**, 390 (1997).
 - [13] A. M. Childs, I. L. Chuang, and D. W. Leung, Phys. Rev. A **64**, 012314 (2001).
 - [14] J. L. O'Brien et al., Phys. Rev. Lett. **93**, 080502 (2004).
 - [15] N. Kiesel, C. Schmid, U. Weber, R. Ursin, and H. Weinfurter, Phys. Rev. Lett. **95**, 210505 (2005).
 - [16] F. Schmidt-Kaler et al., Appl. Phys. B **77**, 789 (2003).
 - [17] A. M. Childs and I. L. Chuang, Phys. Rev. A **63**, 012306 (2000)
 - [18] C. F. Roos et al., Phys. Rev. Lett. **92**, 220402 (2004).
 - [19] F. Schmidt-Kaler et al., J. Phys. B: At. Mol. Opt. Phys. **36**, 623 (2003)
 - [20] M. Ježek and J. Fiurásek and Z. Hradil, Phys. Rev. A **68**, 012305 (2003).
 - [21] W. K. Wootters, Phys. Rev. Lett. **80**, 2245 (1998).
 - [22] A. Steane et al., Phys. Rev. A **62**, 042305 (2000).
 - [23] D. J. Wineland et al., J. Res. Natl. Inst. Stand. Technol. **103**, 259 (1998).